frontiers | Frontiers in Materials

TYPE Original Research
PUBLISHED 27 June 2024
DOI 10.3389/fmats.2024.1381176

OPEN ACCESS

EDITED BY
Ilaria Cacciotti,
University Niccolò Cusano, Italy

REVIEWED BY
Anton Liopo,
Texas A&M Health Science Center,
United States
Vivekanandan Palaninathan,
Toyo University, Japan

*CORRESPONDENCE
Cristina Satriano,
cristina.satriano@unict.it

RECEIVED 03 February 2024
ACCEPTED 28 May 2024
PUBLISHED 27 June 2024

CITATION
Foti A, Clépoint B, Fraix A, D'Urso L, De Bonis A and Satriano C (2024), A simple approach for CTAB-free and biofunctionalized gold nanorods to construct photothermal active nanomedicine for potential *in vivo* applications in cancer cells and scar treatment.
Front. Mater. 11:1381176.
doi: 10.3389/fmats.2024.1381176

A simple approach for CTAB-free and biofunctionalized gold nanorods to construct photothermal active nanomedicine for potential *in vivo* applications in cancer cells and scar treatment

Alice Foti[1], Benjamin Clépoint[2], Aurore Fraix[2], Luisa D'Urso[1], Angela De Bonis[3] and Cristina Satriano[1]*

[1]Department of Chemical Sciences, University of Catania, Catania, Italy, [2]Department of Drug and Health Sciences, University of Catania, Catania, Italy, [3]Department of Sciences, University of Basilicata, Potenza, Italy

Cetyltrimethylammonium bromide (CTAB), a surfactant commonly used in the synthesis of gold nanorods (AuNR), presents challenges owing to cytotoxicity in biological applications, limiting their biomedical applicability, particularly in cancer therapy. This study introduces a straightforward methodology for the effective removal of CTAB by utilizing a combination of ligand replacement and surface bioconjugation processes that efficiently eliminates CTAB and simultaneously functionalizes nanorods with hyaluronic acid (HA) to enhance biocompatibility and introduce targeting capabilities toward cancer cells. The surface chemistry modification of CTAB-capped and CTAB-free AuNR, before and after the functionalization with HA, was scrutinized by UV–visible, surface-enhanced Raman scattering (SERS), attenuated total reflectance (ATR) Fourier-transform infrared (FTIR), and X-ray photoelectron (XPS) spectroscopies. The surface charge, size, and morphology of the different plasmonic nanoparticles were characterized by zeta potential, dynamic light scattering (DLS), and transmission electron microscopy (TEM). The photothermal response was assessed by laser irradiation and thermal camera measurements. Proof-of-work *in vitro* cellular experiments of cytotoxicity and oxidative stress were carried out on prostate cancer cells, PC-3, overexpressing the CD44 cell surface receptor specifically recognized by HA, in comparison with the CD44-negative murine fibroblasts (3T3 cell line) by MTT and MitoSOX assays, respectively. Cellular uptake and organelle alteration were scrutinized by confocal laser scanning microscopy (LSM), while the perturbative effects on cell migration were studied by optical microscopy (wound scratch assay). The study's findings offer a promising pathway to tune the gold nanorod

properties in cancer treatment by reducing cytotoxicity and enhancing targeted therapeutic efficacy, as well as in the control of scar tissue formation.

KEYWORDS

nanomedicine, plasmonic nanoparticles, prostate cancer cells, fibroblasts, wound scratch, hyaluronic acid, photothermal therapy

1 Introduction

Nanomaterials, particularly metal nanoparticles (NPs) (Di Pietro et al., 2016; Liu et al., 2021; Nejabat et al., 2023), have garnered significant interest in recent years for their potential as therapeutic and diagnostic tools (theranostics). Their dimensions, typically ranging from 1 to 100 nm, align closely with the scale of cellular organelles, thereby enabling unique interactions with various biological pathways (Villanueva-Flores et al., 2020). Noble metal NPs, for instance, possess extraordinary physicochemical properties (e.g., optical, electrical, photothermal, and high surface area) that can be exploited for different applications in sustainable environmental management as well as in biomedicine, such as carriers for drug delivery, agents for photothermal therapy, imaging agents, or even radiosensitizers in radiation, proton, and photodynamic therapy (Anselmo and Mitragotri, 2016; Naletova et al., 2019).

Among the myriad of NPs investigated in the last decades as potential nanomedicine tools, gold nanorods (AuNR) are exceptional due to their anisotropic nature, which results in two distinct localized surface plasmon resonance (LSPR) bands. These bands are generated by light absorption along their short (transverse) and long (longitudinal) axes, with the longitudinal plasmon resonance band being modulable by altering the aspect ratio of nanoparticles (Bouhelier et al., 2005) to reach the near-infrared (NIR) region, i.e., in overlap with the optical window of biological tissues, which is very convenient for thermal ablation of cancer cells (Nejabat et al., 2023).

Gold nanoconstructs are slowly but steadily transitioning into clinical trials (Zhang et al., 2022); however, for their effective and safe translation from bench-to-bedside, still some burdens need to be wrecked, including long-term and accumulation of toxicity (in the case of prolonged treatments), pharmacokinetic behaviors (i.e., half-life and clearance rate), and tissue distribution (Yao et al., 2023). Therefore, it becomes essential to tailor size, shape, and surface functionalities, which in turn affect the charge and cellular uptake of nanoparticles, to fulfill the requested criteria for such applications. For example, it is critically important to have a high absorption cross-section, which results in effective photothermal heating close to the nanoparticle within a wavelength range that is compatible with physiological conditions (Pérez-Juste et al., 2005; Cole et al., 2009).

Many synthetic approaches have been extensively studied and tuned for construction of anisotropic nanomaterials to achieve certain morphologies and optimized aspect ratios. However, conventional seed-mediated synthesis still suffers a certain number of limitation/flaws, including the reproducibility, poor yield of ionic-to-metallic gold conversion (Vigderman and Zubarev, 2013), and toxicity. The chemical route of synthesis particularly for rod-shaped Au NPs requires the use of toxic surfactants such as cetyltrimethylammonium bromide (CTAB) in excess stoichiometry, which provides a micellar environment that promotes the anisotropic growth of Au seeds in certain directions (Tomasella et al., 2020; Wittmann et al., 2023). CTAB toxicity is mainly due to the impairment of the cell membrane and inhibition of ATP synthase, both leading to cell death (Johnson et al., 2002). An established strategy to remove CTAB from the suspension is to centrifugate and wash the NRs, with the limitations of of potential aggregation and no effective removal from the nanorod surface. Other established methods for CTAB removal from the AuNR surface include ligand exchange with biocompatible molecules, such as polyethylene glycol (PEG) (Niidome et al., 2006) and thiolated polyamidoamine (PAMAM) (Li et al., 2009). A facile synthesis for CTAB removal was proposed by He J. et al., consisting in a first addition of sodium borohydride to remove CTAB, given its great affinity to gold surface, followed by ligand replacement with mercaptoundecanoic acid (MUA) (He et al., 2018).

Our approach extends upon the framework proposed by He et al., by introducing adaptations tailored to optimize the biocompatibility, biodegradation, moisture retention, and anti-inflammatory properties of AuNRs. For this purpose, the ligand exchange reaction with sodium borohydride was followed by the addition of hyaluronan (HA), also called hyaluronic acid or hyaluronate. HA is the main non-protein glycosaminoglycan component of the extracellular matrix (ECM) (Garantziotis and Savani, 2019), with anti-inflammatory properties that, thanks to its structure, i.e., repeating glucuronic acid and N-acetylglucosamine units, enhance moisture retention and biocompatibility (Della Sala et al., 2022). HA also has cancer-targeting capability, mediated by the CD44 cell-surface receptor (Luo et al., 2019), which has been shown to play a key role in prostate cancer metastasis, migration, and invasion (Senbanjo et al., 2019). HA has been used as a bioactive scaffold in nano-biointerface studies (Greco et al., 2020; Palomba et al., 2020; Sanfilippo et al., 2020).

We investigated the removal of CTAB from AuNRs and their concurrent biofunctionalization with HA in terms of the plasmonic properties and resulting changes in the photothermal response of the nanoparticles. Proof-of work *in vitro* cellular experiments of cytotoxicity and cell migration were carried out on prostate cancer cells (PC-3 line) in comparison with fibroblast cells (NT-3 line), highlighting the very promising potential of this method for effective application of gold nanorods in nanomedicine.

2 Materials and methods

2.1 Chemicals

Gold (III) chloride trihydrate ($HAuCl_4$) purity ≥99.9%, cetyltrimethylammonium bromide (CTAB), silver nitrate ($AgNO_3$), L-ascorbic acid purity ≥99%, and sodium borohydride ($NaBH_4$)

were provided by Sigma-Aldrich (St. Louis, MO, USA). Sodium hyaluronate (HA-200 kDa) was a kind gift from Fidia Farmaceutici S.p.A (IT). For cellular experiments, Dulbecco's modified Eagle medium (DMEM/F-12), RPMI-1640, penicillin–streptomycin, L-glutamine, fetal bovine serum (FBS), dimethyl sulfoxide (DMSO), Dulbecco's phosphate-buffered saline (PBS), and 3-(4,5-dimethylthiazol-2-yl)-2,5-diphenyltetrazolium bromide (MTT) were purchased from Sigma-Aldrich (St. Louis, MO, USA). Ultrapure Milli-Q water was used (18.2 mΩ cm at 25°C, Millipore), and the glassware was cleaned with aqua regia (HCl: HNO_3 3:1 volume ratio) and rinsed with ultrapure water before each use. MitoSOX Red mitochondrial superoxide indicator for live-cell imaging, MitoTracker Deep Red, LysoTracker Red, and Hoechst were purchased from Thermo Fisher Scientific (Waltham, Massachusetts, United States).

2.2 Synthesis of gold nanorods

Aqueous AuNR dispersions were obtained by the seed-mediated growth method. Seeds (Seed@CTAB) were prepared as follows: 25 μL of 50 mM $HAuCl_4$ was added to 4.7 mL of 0.1 CTAB solution in a 29°C water bath under gentle stirring. After 5 min, 300 μL of freshly prepared 10 mM $NaBH_4$ was added to the solution and stirred for 5 min, until the color turned to brown–yellow. The growth solution was prepared by adding 100 μL of 50 mM $HAuCl_4$ to 10 mL of 0.1 M CTAB solution under stirring for 10 min in a 29°C water bath, followed by the addition of 76 μL of 100 mM ascorbic acid (solution turned colorless) and 100 μL of 5 mM $AgNO_3$. Finally, 106 μL of Seed@CTAB was added, and the solution was vigorously stirred at 279°C for 15 min. The change in color was observed at the end of this time. The obtained colloidal dispersion was purified by removing reactants' excess through two centrifugation steps (8000 × rpm, 30 min, 29°C), with water washing performed in between to obtain the sample named "pellet 2." To calculate the actual concentration of the AuNR dispersion, Eq. 1 was used to find the molar extinction coefficient ε (nM^{-1} cm^{-1}):

$$\boldsymbol{\varepsilon = 1.2\lambda_{max} - 4.8}, \tag{1}$$

where λ_{max} is the maximum absorption of the longitudinal plasmon resonance SPR peak (Orendorff and Murphy, 2006), whose position is affected, with a linear dependence, by the aspect ratio (AR) value, calculated according to Eq. 2 (Govindaraju et al., 2019):

$$\boldsymbol{\lambda_{max} = 95(AR) + 420}. \tag{2}$$

2.3 CTAB removal from AuNRs and bioconjugation with HA

A 2 mL volume of AuNR (A = 1), typically aged for 24 h since the purification, was treated with 2.25 mM (final concentration) $NaBH_4$ for 30 min. Afterward, the dispersion was purified by removing reactants' excess through two centrifugation steps (8,000 × rpm, 10 min, 29°C), with water washing performed in between to obtain the sample "pellet 4" (see Supplementary Figure S1). Five microliters of HA (200 kDa molecular weight) stock solution (1% w/v) in Milli-Q H_2O was added dropwise to samples "pellet 2" and "pellet 4" to obtain AuNR (+CTAB)/HA and AuNR (-CTAB)/HA, respectively.

2.4 Physicochemical and functional characterization of CTAB-capped and CTAB-free AuNR

AuNR (+CTAB) (pellet 2), AuNR (-CTAB) (pellet 4), AuNR (+CTAB)/HA (pellet 2+ HA $1.25{\cdot}10^{-6}$ M), and AuNR (-CTAB)/HA (pellet 4+ HA $1.25{\cdot}10^{-6}$ M) samples were analyzed in terms of plasmonic and photothermal properties, chemical structure, surface charge, and morphology.

2.4.1 UV–visible spectroscopy

UV–visible spectra of the aqueous dispersions of AuNR were collected by using quartz cuvettes with optical path lengths of 1 and 0.1 cm on a PerkinElmer UV–vis spectrometer (Lambda 2S, Waltham, MA, United States).

2.4.2 Attenuated total reflectance FTIR spectroscopy (ATR-FTIR)

FTIR Imaging System PerkinElmer Frontier Spotlight 400 equipped with a germanium crystal was used for Fourier-transform infrared spectroscopy-attenuated total reflection (FTIR-ATR) data collection (Spotlight 400 software). A 20-μL drop of the sample being investigated was directly placed on the ATR crystal, and all FTIR-ATR spectra were recorded from 4,000 to 550 cm^{-1} at a spectral resolution of 1 cm^{-1} and 20 number of scans. Before each sample analysis, a background spectrum, by adding 20 μL of Millipore MQ water on the ATR crystal, was taken as the reference.

2.4.3 Nanoparticle tracking analysis (NTA) and zeta potential (ZP)

Size and concentration measurements were performed using the nanoparticle tracking analysis (NTA) technique on a NanoSight NS 500 instrument (Malvern Panalytical, Malvern, UK). The concentration is established after consistent measurements of the sample used as such and diluted 2 X using Milli-Q water (see illustration videos Supplementary Material, where bright dots represent the light scattered by NPs and do not give direct information about the size; difference of brightness can be due to the different nature of the coating surrounding the metallic NPs). ZP measurements were carried out with a ZetaSizer NanoZS90 Malvern Instrument (Malvern, UK).

2.4.4 Raman spectroscopy

Raman scattering was observed by using an excitation wavelength of 785 nm radiation with a diode laser (Xtra II high-power single-frequency diode laser—Toptica Photonics) and analyzed by a WITec alpha 300 (Wissenschaftliche Instrumente und Technologie GmbH, Ulm, Germany) confocal Raman apparatus. Spectra were collected with a ×100 objective (spot size of ≈1 μm). To operate in an SERS regime, the laser excitation wavelength was chosen near the spectral position of the localized surface plasmon resonance (LSPR) maximum of the gold nanorods.

2.4.5 X-ray photoelectron spectroscopy

Nanoparticles collected onto a silicon (100) wafer were used for XPS measurements. Spectra were collected by using the SPECS Phoibos 100-MCD5 spectrometer operating at 100 W in FAT (fixed analyzer transmission) equipped with Mg Kα (1,253.6 eV) achromatic radiation and with a channel width of 0.1 eV.

2.4.6 Transmission electron microscopy

For TEM analysis, few drops of the colloidal solutions were casted on Holey carbon film-supported copper grids. TEM images were acquired by using an FEI TECNAI G2 microscope operating at 200 kV.

2.4.7 Laser irradiation and thermal camera measurements

For the photothermal measurements, 100 µL volume of each sample was placed in an NMR tube and irradiated with a continuous-wave (CW) laser, 671 nm at 250 mW, with a beam diameter of ca. 1.5 mm. The evolution of the temperature was followed in real-time using an FLIR C3 thermal imaging camera.

2.5 Cellular experiments

2.5.1 Cell cultures and maintenance

The mouse fibroblast 3T3 cell line was cultured in DMEM/F-12 medium, and the prostate cancer PC-3 cell line was cultured in RPMI-1640. Both mediums were supplemented with 10% v/v fetal bovine serum (FBS) and contained 2 mM L-glutamine, 50 IU/mL penicillin, and 50 µg/mL streptomycin. Cells were grown in tissue culture-treated Corning® flasks (Sigma-Aldrich, St. Louis, MO, United States) in an incubator (Heraeus Heracell 150C incubator), under a humidified atmosphere at 37°C in 5% CO_2.

2.5.2 Cell viability and reactive oxygen species production

For the assessment of AuNR cytotoxicity and oxidative stress production, cells (3T3 and PC-3 at passages 14 and 11, respectively) were seeded at a density of 10,000 cells/well in a 96-well plate and maintained in their respective complete media in standard culture conditions. The next day, the cells were washed with 1% FBS-supplemented medium and treated with different sample concentrations (dilutions from 50 X to 200 X). Cells untreated and cells treated with HA were included as negative and positive controls, respectively. After 24 h of treatment, the cells were washed with PBS. For the MTT assay, cells were incubated with 5 mg/mL of 3-(4,5-dimethyl-2-thiazolyl)- 2,5-diphenyl-2H-tetrazolium bromide (MTT) at 37°C for 180 min. The formazan salts formed by succinate dehydrogenase activity in live cells were solubilized with DMSO, and viable cells were quantified by monitoring the absorbance value at 570 nm of wavelength on a Synergy 2 microplate reader (BioTek, Winooski, VT, United States). For the ROS production assay, cells were stained by treatment at 37°C for 15 min with 5 µM MitoSOX and 0.12 µg/mL (λex/em = 396/580 nm) and Hoechst 33342 (λex/em = 361/460 nm) dyes. For ROS estimation, the fluorescence values of MitoSOX signals were normalized to the Hoechst 33342 emission. All conditions were measured in triplicate, and the results were expressed as percentage of the negative control (i.e., untreated cells).

2.5.3 Wound scratch assay

The perturbation in the migration capabilities of cancer cells (PC-3 line) induced by the treatment with AuNR (+/-CTAB)/HA samples was assessed with a wound scratch assay. The cells were seeded in a 48-well plate and maintained in their respective complete media in standard culture conditions for 48 h to achieve 100% of monolayer confluency. The monolayer wounding was performed by gently scratching with a 10-µL plastic pipette tip. Any cellular debris was rinsed with complete medium. Afterward, the cells were treated with samples (50 X and 100 X dilution, including negative and positive controls). After 24 h of treatment, the cells were washed with PBS, and serial phase-contrast images (Leica) were taken immediately after the treatment and at regular time intervals up to 48 h of incubation. The width of the separation wall was measured by using ImageJ software.

2.5.4 Laser scanning confocal microscopy

Cells were plated at a density of 15,000 cells/dish in complete medium in 12-mm-diameter glass bottom dishes (WillCo-dish®, Willco Wells, B.V.). The next day, the cells were washed with 1% FBS-supplemented medium and treated with different sample concentrations (100 X dilution). Cells untreated and cells treated with HA ($1.25{\cdot}10^{-8}$ M) were included as negative and positive controls, respectively. After 2 h of treatment, the cells were washed with PBS, and the nuclei, lysosomes, and mitochondria were stained with Hoechst 33342 (1 µg/mL), LysoTracker Red ($3{\cdot}10^{-7}$ M), and MitoTracker Deep Red ($2{\cdot}10^{-7}$ M), respectively. After 15 min of incubation with dye molecules, the cells were washed with PBS and fixed with high-purity paraformaldehyde (2% in PBS, pH = 7.3). Confocal laser scanning microscopy acquisitions were collected on a Leica microscope (TCS SP8 model) using an HCX PL APO CS2 63 × 1.40 NA oil immersion objective lens (Leica Microsystems, Mannheim, Germany). Laser sources with excitation wavelengths of 405, 567, and 633 nm were used to detect emission spectra in the wavelength regions of 425–475 nm (Hoechst), 570–620 nm (LysoTracker), and 650–600 nm (MitoTracker), respectively. The pinhole size was set to 1 Airy unit. Transmitted light images were acquired simultaneously using a transmitted light detector (TLD) to visualize the morphology of the cells. The confocal fluorescence images were enhanced by deconvolution using Huygens Essential X11 software version 23.10 (Scientific Volume Imaging, Netherlands, http://svi.nl), and the quantitative analysis of intensity for lysosome and mitochondria staining was analyzed with respect to the intensity of the negative control (untreated cells).

3 Results and discussion

The LSPR peak features of AuNRs before and after CTAB removal were investigated by UV–visible spectroscopy in the comparison with TEM analyses (Figure 1). The spectra in Figure 1A for the CTAB-capped AuNR show the expected features of rod-shaped nanoparticles, with evidence of two absorption bands, the most intense one in the NIR region (~800 nm), due to electron oscillations along the long axis, referred to as the longitudinal band (λ_L), and a lower band in the visible region (~512 nm), generated by electron oscillation along the transverse axis (λ_T), with absorbance maximum at a wavelength comparable to that of

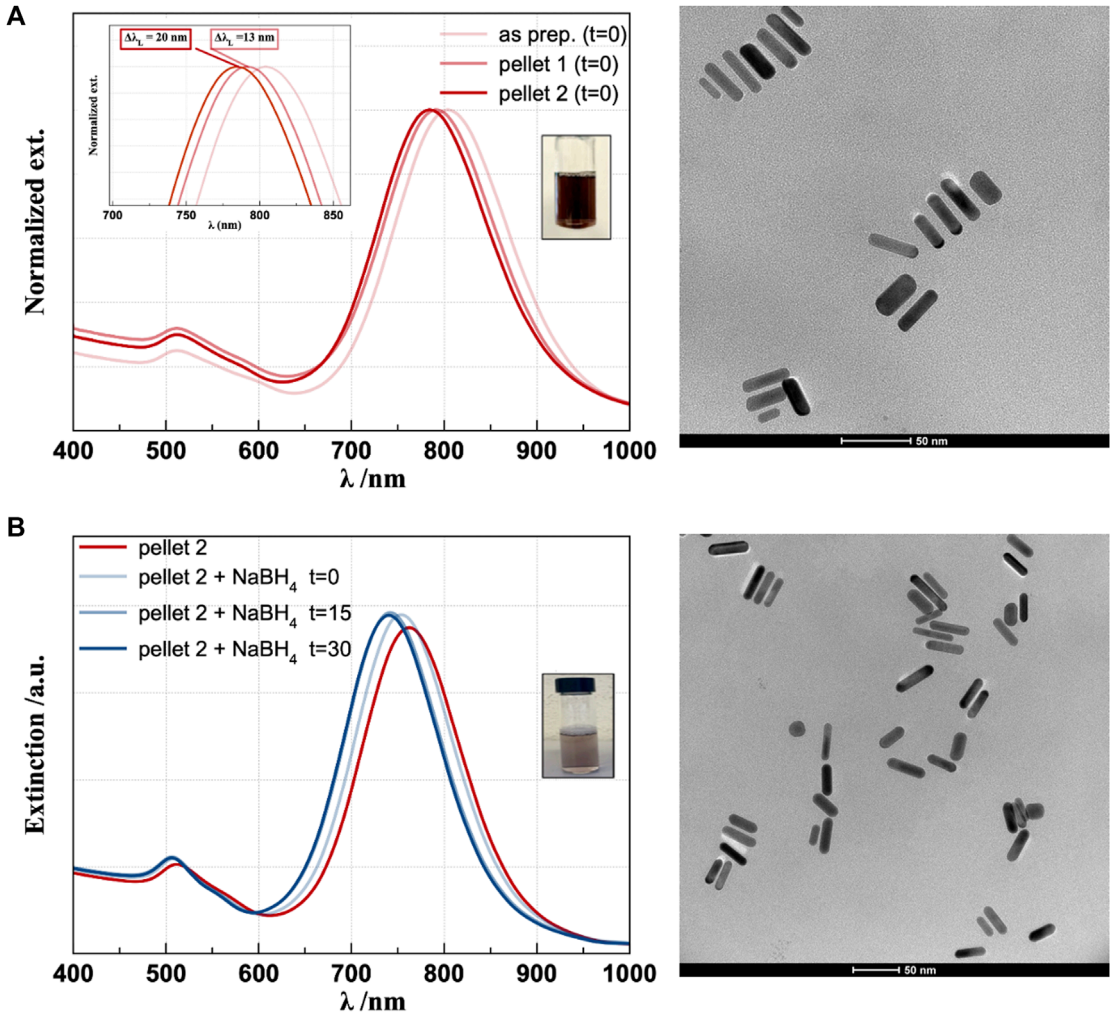

FIGURE 1
UV–visible spectra and TEM micrographs of CTAB-capped **(A)** and CTAB-free **(B)** gold nanorods.

TABLE 1 LSPR values, calculated aspect ratio (AR), and concentration (C) for AuNR.

Sample	λ_T (nm)	A_T	λ_L (nm)	A_L	AR	C (nM)
AuNR as prepared	513	0.1	804	0.4	3.9	0.8
AuNR pellet 1	512	0.8	791	2.5	3.8	5.3
AuNR pellet 2	512	0.7	784	2.5	3.7	5.3

spherical gold approximately 10 nm in diameter (Foti et al., 2023). In the inset of Figure 1A is displayed the magnified view of longitudinal band shifts. The spectral parameters of the plasmon bands, i.e., wavelengths, and the correspondent absorbance values are reported in Table 1, together with the calculated aspect ratio and nanoparticle concentration, according to Eqs 1, 2 (see Supplementary Methods). The data in Table 1 evidence a relatively high stability of the nanorods upon the purification process done by centrifugation, with the transversal plasmonic band being practically unmoved and a blue shift for the longitudinal band of ~20 nm, which still falls in the NIR region. As per the purified CTAB-capped AuNR (pellet 2 sample), the calculated aspect ratio from the LSPR peak analysis (AR = 3.7) is comparable to the value measured by TEM (AR = 4), corresponding to the average size of 9 (±2) nm and 33 (±3) nm for the short and long axes, respectively.

The spectra in Figure 1B allow following the process of ligand exchange during the treatment with $NaBH_4$ up to 30 min from the beginning of the reaction. In particular, hypsochromic shifts of ~20 nm and ~5 nm for λ_L and λ_T, respectively, were observed (Table 2), in agreement with the evident smaller features observed in the TEM micrographs of CTAB-free (Figure 1B) than CTAB-capped AuNR (Figure 1A). The average transversal and longitudinal

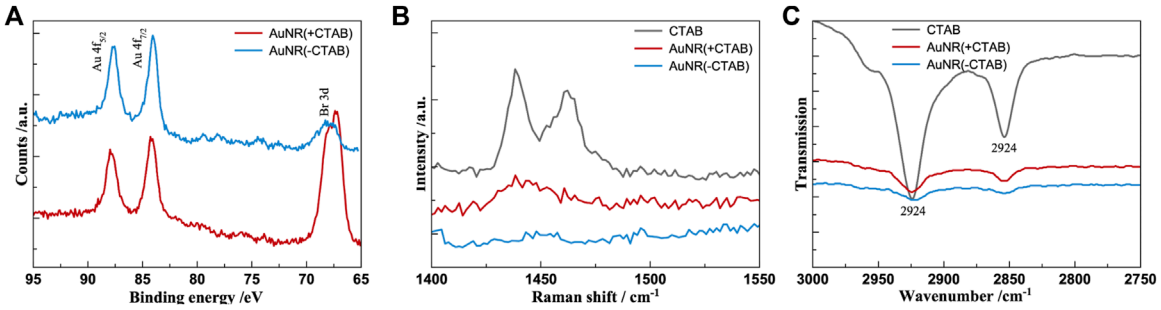

FIGURE 2
XPS **(A)**, Raman-SERS **(B)**, and ATR-FTIR **(C)** spectra of CTAB-capped (red) and CTAB-free (blue) gold nanorods. The vibrational spectrum of CTAB (gray) is included for comparison.

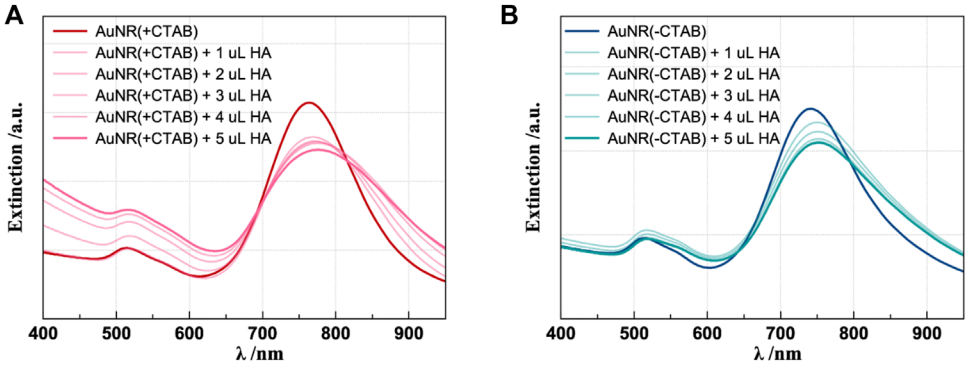

FIGURE 3
UV–visible spectra of HA 1% (w/v) addition to CTAB-capped **(A)** and CTAB-free **(B)** AuNRs. The spectra of the correspondent samples before HA addition are shown as the reference (darker lines).

TABLE 2 LSPR values, calculated aspect ratio (AR), and concentration (C) for AuNR pellet 2 before (red) and after (dark blue) $NaBH_4$ addition.

Sample	$\Delta\lambda_T$ (nm)	A_T	$\Delta\lambda_L$ (nm)	A_L
AuNR pellet 2 + $NaBH_4$ t = 0	−3	0.3	−9	1
AuNR pellet 2 + $NrojaBH_4$ t = 15′	−4	0.3	−20	1
AuNR pellet 2 + $NaBH_4$ t = 30′	−5	0.3	−23	1

TABLE 3 Results of NTA, with the values of the NP concentration and hydrodynamic diameter measured by utilizing the properties of both light scattering and Brownian motion of the nanoparticles. In the last column, the surface charges of the different samples from ZP measurements are reported.

Sample	Particle concentration (NP/mL)	Hydrodynamic diameter (nm)	ZP (mV)
AuNR (−CTAB)	$4.0{\cdot}10^9$	31	−7.7 ± 1.5
AuNR (−CTAB)/HA	$1.2{\cdot}10^9$	77	−27.6 ± 3.2
AuNR (+CTAB)		63	7.7 ± 0.7
AuNR (+CTAB)/HA		84	2.5 ± 2.8
HA			−13.4 ± 1.6

dimensions calculated from TEM for the CTAB-free nanorods are 6 (±1) nm and 26 (±3) nm. Such a "shrinking" of the NPs can be explained considering the mechanism of CTAB-assisted growth of Au seeds, involving a rod-shaped micellar bilayer formed by the surfactant, where the polar heads on the one end adsorb on gold and on the other end interact with water (Meena and Sulpizi, 2013). Molecular dynamics simulations discriminated between the arrangements of CTAB adsorbing onto flat or curved Au surfaces, with a lower CTAB coverage density and larger inter-micellar channels found on curved surfaces (representing the tip facets of growing AuNR) compared to those on a flat surface (representing the lateral facets of growing AuNR) (da Silva et al., 2019). By inferring a similar mechanism for CTAB removal (i.e., desorption process from the gold surface), one can hypothesize that the decreased CTAB concentration affects tip facets more than the lateral facets, resulting in decreased aspect ratio. Furthermore, CTAB removal from the AuNR surface leads to a reduction in the

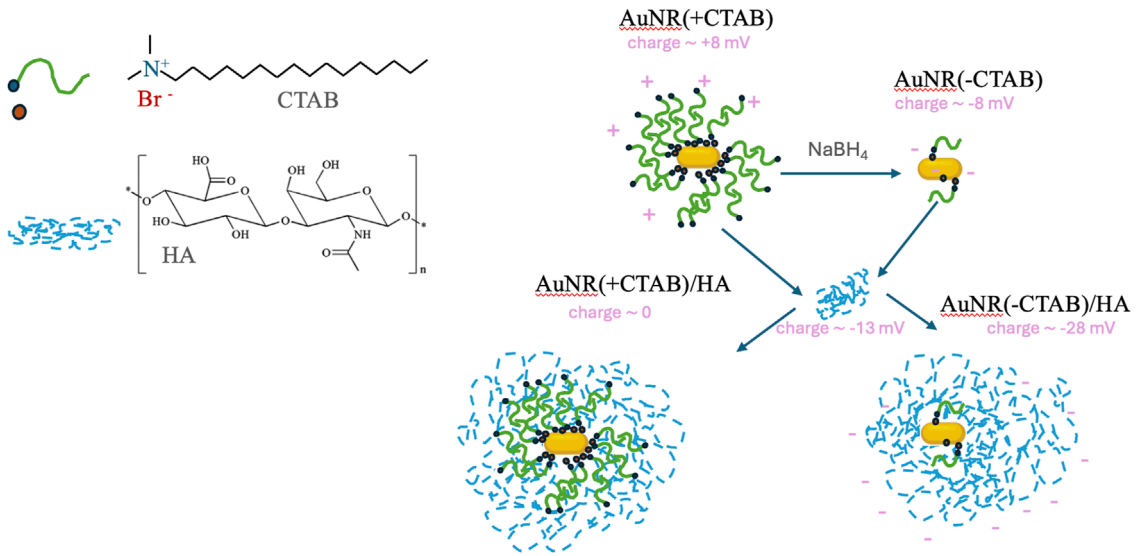

FIGURE 4
Schematic representation of Au (+/−CTAB)/HA samples figured out according to the surface chemical structure and charge analyses of the nanorods.

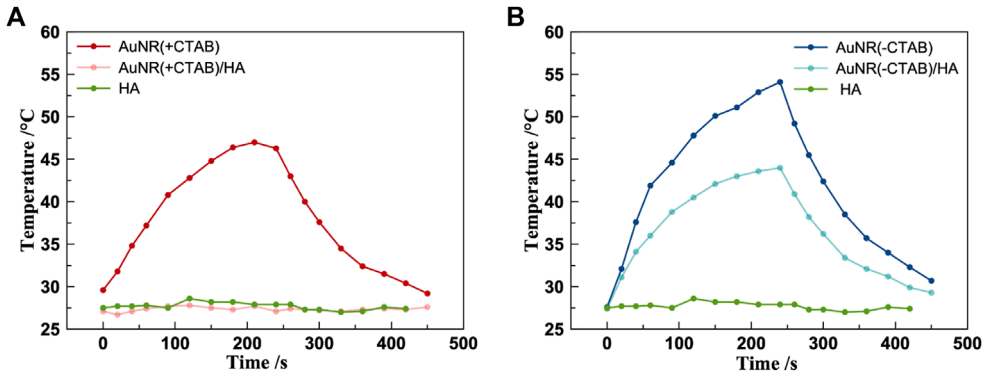

FIGURE 5
Photothermal measurements of AuNR (+CTAB)/±HA **(A)** and AuNR (−CTAB)/±HA **(B)**. (CW laser 671 cm, 250 mW, beam diameter 1.5 mm).

refractive index (1.44 for CTAB and 1.33 for water), which is in agreement with the blue shift observed in the longitudinal band (Casas et al., 2013; Movsesyan et al., 2019).

The XPS, Raman, and FTIR spectra of the CTAB-capped and CTAB-free AuNR (Figure 2) confirm the effective removal of the surfactant by treatment with $NaBH_4$. Figure 2A shows that the Br $3d_{5/2}$ signal, centered at a binding energy of 64.3 eV, which points to the presence of Br^- species, is strongly decreased in CTAB-free AuNR compared to CTAB-capped nanorods. Moreover, the Au $4f_{7/2}$ signal, centered at 84.0 eV in both spectra, confirms the formation of metallic gold (Oliveira et al., 2021). The Au/Br atomic ratio was evaluated to be 0.1 and 0.66 for CTAB-capped and CTAB-free AuNR, respectively, thus confirming the effective removal of the surfactant by treatment with $NaBH_4$. In Figure 2B, the spectrum of AuNR (+CTAB) (red line) in the 1,040–1780 cm^{-1} range shows strong CTAB-characteristic Raman vibrational bands (gray line) at 1,057 cm^{-1} (C-C stretch), 1,124 and 1,293 (C-C stretching and CH_2 twist), and 1,425 and 1,478 cm^{-1} (the combination of CH_2 scissors and CH_3 deformations) (Gökce and Bahçeli, 2013). In the spectrum of AuNR (-CTAB) (blue line), such bands totally disappear, confirming the formation of an almost CTAB-free surface suitable for subsequent functionalization with hyaluronic acid. Accordingly, the ATR-FTIR spectra (Figure 2C) display for the CTAB-free AuNR an evident decrease of the strong absorptions at 2,924 and 2,854 cm^{-1} due to C–H stretching vibration of methyl and methylene groups of CTAB, respectively (Su et al., 2015).

Concerning the HA-functionalized AuNR, both AuNR (+CTAB)/HA and AuNR (-CTAB)/HA samples, the UV–visible spectra (Figure 3) show evidence of effective polymer coating, with similar bathochromic shifts of the plasmon bands ($\Delta\lambda_T$ = + 3 nm; $\Delta\lambda_L$ = + 12–13 nm) found for both CTAB-capped (Figure 3A) and CTAB-free AuNR (Figure 3B), as expected

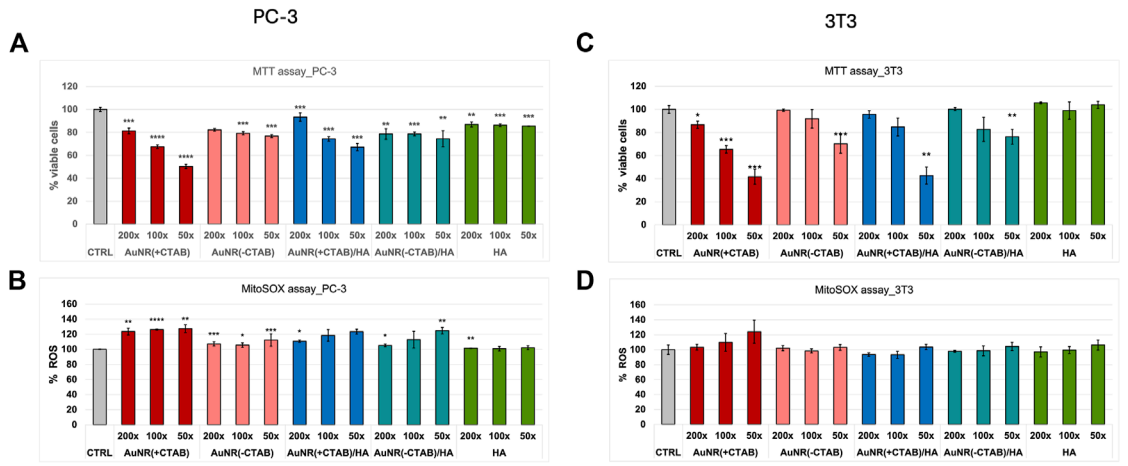

FIGURE 6
Cell viability (MTT assay; a,c) and ROS production analysis (MitoSOX assay; b,d) in PC-3 **(A, B)** and 3T3 **(C, D)** cells after 24-h incubation with CTAB-capped AuNR w/o HA and CTAB-free AuNR w/o HA samples. Negative (untreated cells, CTRL) and positive (HA-treated cells) controls are included. The results are expressed as average values ± SEM from three independent experiments. Statistical analysis was performed by pairwise Student's t-test. (*) $p < 0.05$, (**) $p < 0.01$, (***) $p < 0.001$, (****) and $p < 0.0001$ vs. CTRL.

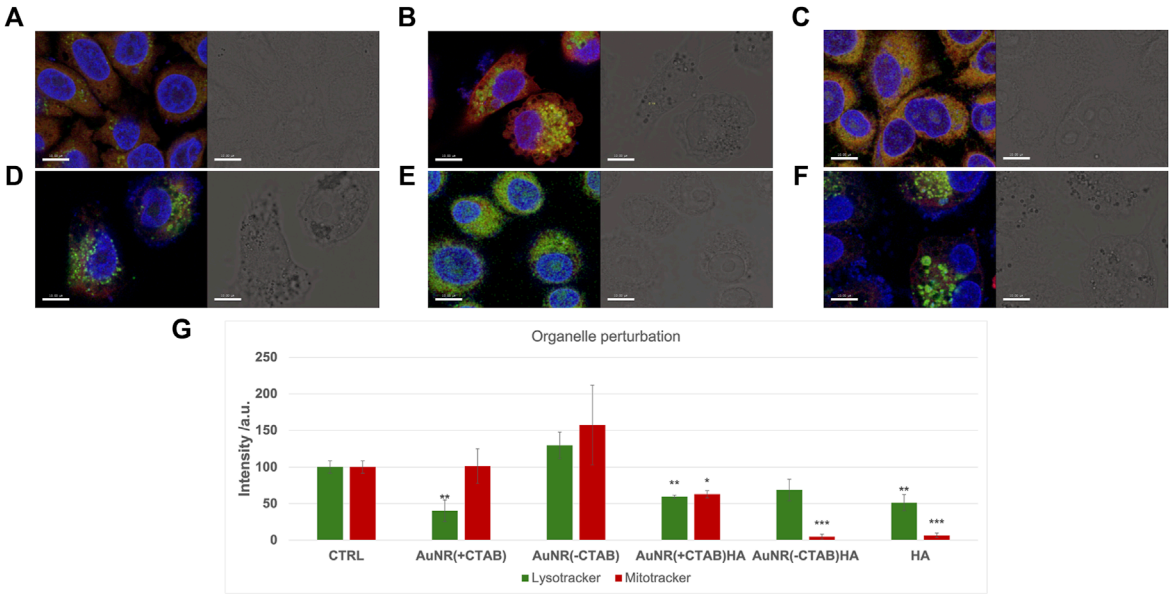

FIGURE 7
LSM micrographs (scale bar = 10 μm) of PC-3 cells untreated **(A)** or 2 h treated with **(B)** AuNR (+CTAB), **(C)** AuNR (-CTAB), **(D)** HA, **(E)** AuNR (+CTAB)/HA, and **(F)** AuNR (-CTAB)/HA. Left hand panels: merged confocal images in false colors of stained nuclei/lysosomes/mitochondria (blue/green/red). Right hand panels: brightfield micrographs. **(G)** Quantitative analysis of emission for lysosome and mitochondria staining. The results are expressed as average values ± SEM from three independent experiments. Statistical analysis was performed by pairwise Student's t-test. (*) $p < 0.05$, (**) $p < 0.01$, and (***) $p < 0.001$ vs. CTRL.

for the plasmonic signals of nanoparticles that increase their optical size due to the physisorption of the hyaluronan molecules (Sanfilippo et al., 2020). Normal Raman and SERS spectra of HA-functionalized nanoparticles were collected and compared to those of pure HA for comparison and peak assignment following the literature (Cannavà et al., 2022). A sole band around 1,040 cm^{-1} resulting from overlap of the C-C and C-O stretching modes is observed in both HA and HA-functionalized AuNR samples, therefore confirming the success of the interaction (Supplementary Figure S2).

NTA analyses, which allow particle-by-particle analysis, provided the NP concentration of the sample after CTAB removal and successively after HA addition (Table 3). The similar values found of $4.0\ 10^9$ and $1.2\ 10^9$ NP mL^{-1} demonstrate that the treatment does not induce drastic changes, such as precipitation, in the solution. Table 2 reports also the values of hydrodynamic

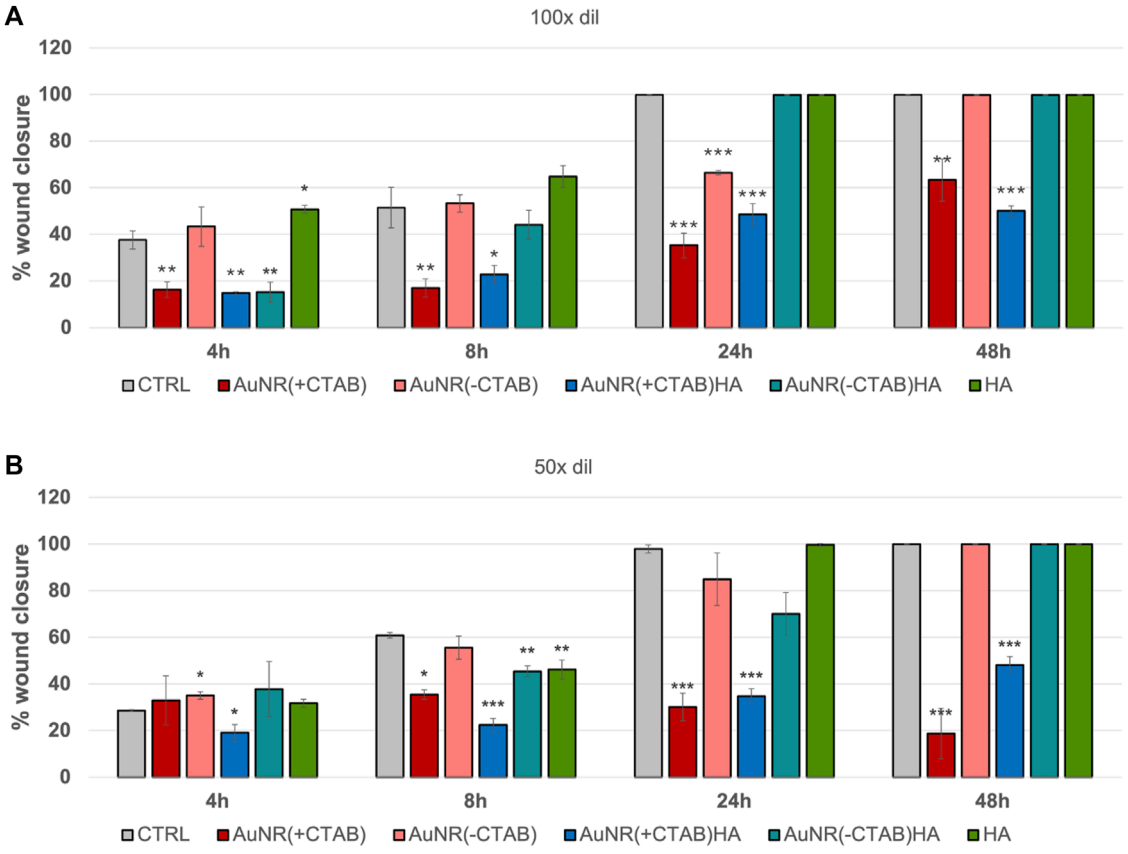

FIGURE 8
Quantitative analysis of migration assay for PC-3 cells after 4, 8, 24 and 48 h incubation with **(A)** 100 X dilution and **(B)** 50 X dilution of AuNR (+/−CTAB) and AuNR (+/−CTAB)/HA samples. The negative (CTRL, untreated cells) and positive (HA-treated cells) are included for comparison. The results are expressed as average values of wound edge advancement in percent vs time 0 ± SEM from three independent experiments. Statistical analysis was performed by pairwise Student's t-test. (∗) $p < 0.05$, (∗ ∗) $p < 0.01$ and (∗ ∗ ∗) $p < 0.001$ vs. CTRL.

diameter and reveals that the particles without CTAB are smaller than the particles coated with CTAB, according to TEM analyses; furthermore, the presence of HA increases the particle dimension. A further confirmation of effective CTAB removal from the surface of gold nanorods and NP bioconjugation with HA was also obtained from the ZP values from the surface charge analysis of the nanorods, pointing to the neutralization of charges in AuNR (+CTAB)/HA and the negative surface charge on AuNR (-CTAB)/HA, as depicted in Figure 4.

The thermoresponsive properties of AuNR (±CTAB)/±HA were investigated by irradiation with a 671-nm continuous-wave laser (CW), and the trend is shown in Figure 5 (thermographic images of the samples recorded before and after 4 min of irradiation at 671 nm are reported in Supplementary Figure S3). The AuNR samples present a rapid increase in temperature during the 4-min irradiation, except the AuNR (+CTAB)/HA, which precipitated during the experiments and HA alone, showing no response to laser irradiation. In particular, $\Delta T = 27°C$ for AuNR (+CTAB) (Figure 5A) and $\Delta T = 17°C$ for AuNR (-CTAB)/HA (Figure 5B) were observed. Thus, the hybrid system with HA is less responsive than the CTAB-free AuNR alone but reaches a temperature increase like the CTAB-capped sample, suggesting that it is possible to take advantage of the HA desirable bioproperties while preserving photothermal properties almost identical to those observed with the toxic CTAB-capped AuNRs.

The cytotoxicity and oxidative stress of CTAB-capped and CTAB-free AuNR hybrids with HA were tested *in vitro* in fibroblasts (3T3 cell line) and prostate cancer (PC-3, tumor cell line) by MTT and MitoSOX assays, respectively (Figure 6).

In the cell viability assay, for AuNR (+CTAB), a dose-dependent toxic effect of CTAB was evident, as expected from literature data (Jia et al., 2020), with IC_{50} values reaching for the highest treatment dose (i.e., 50x dilution of the AuNR pellet 2) for both PC-3 (Figure 6A) and 3T3 (Figure 6C) cell lines. In the case of AuNR (+CTAB)/HA, a similar trend in the dose–response effect is visible, with a general reduction in toxicity (IC_{50} values above the dose treatment with 50x dilution only for the non-tumoral, CD44-negative cells), which is mitigated by the beneficial presence of the hyaluronan. Noticeably, the AuNR (-CTAB) and AuNR (-CTAB)/HA samples show null or minimal toxicity (~20% reduction), with the dose–response effect visible only for the non-tumoral cells, confirming the success of CTAB removal procedure discussed above.

For ROS production, while no significant oxidative stress induction was detected in 3T3 (Figure 6D), PC-3 cells were found to be the significantly affected by the treatments (Figure 6B). Again, CTAB-capped nanoparticles produce a higher level of oxidative stress than CTAB-free nanoparticles, in agreement with literature data concerning the toxic effects of AuNR that can be attributed to mitochondrial impairment (Bidian et al., 2023). Indeed, AuNRs have been demonstrated to selectively accumulate in the tumoral cell mitochondria, causing their death, while this effect was null on normal cells (3T3, in our case) (Zhang et al., 2013).

The LSM analysis of PC-3 cells upon treatment with the different samples, although not allowing for the visualization of nanoparticles uptake, for instance, nanoparticle aggregates into the cytoplasm clearly visible from the bright field micrographs, gives, however, clear evidence of cellular changes in terms of both cell morphology as well as perturbation of intracellular organelles (Figure 7). Indeed, a significant decrease in the mean fluorescence intensity of stained lysosomes was found in cells incubated with CTAB-capped nanoparticles, while no significant changes were detected in the emission of dye-labeled mitochondria. According to the short incubation time (2 h) used in LSM imaging experiments, our findings are well in agreement with literature data about the special sensitivity of cancer cells to CTAB, which, as a quaternary ammonium cation, can destroy the lysosomal membrane and be further released into the cytoplasm for further targeting of the mitochondria (Wang et al., 2011). On the other hand, the PC-3 cells incubated with AuNR (-CTAB) showed a significant increase in both lysosomal and mitochondrial emission, thus confirming that cellular trafficking of AuNRs in cancer cells is strongly affected by the CTAB concentration. Interestingly, the treatment of cells with HA, which decreases the average emission of stained lysosomes and especially that of the mitochondria, according to the activation of the CD44 receptor by HA and apoptosis regulation by the mitochondrial pathway (Michalczyk et al., 2022), is also observed in cells treated with AuNR (-CTAB)/HA, with comparable decreases in the fluorescence intensity with respect to the negative control of stained lysosomes and the mitochondria of approximately 50%–70% and 5%–6%, respectively.

Figure 8; Supplementary Figure S4 present data from the scratch assay conducted on PC-3 cells over a 48-h timeframe period to evaluate the effects of AuNR (±CTAB)/±HA on cell migration. While both negative and positive control scratches reach 100% of wound closure after 24 h, all the treatments with the gold nanorods inhibit cancer cell migration. As expected, the two samples with CTAB prevent cellular migration, paralleling the toxic effect evidenced by the MTT assay. On the other hand, the cell treatments with CTAB-free nanorods showed a reduction in cell migration, which is not as high as that observed in the CTAB-capped nanorods, confirming that AuNRs possess intrinsic anti-tumoral properties, even if the toxic surfactant is removed from the surface, in accordance with the cytotoxicity tests. These findings are particularly promising since controlled inhibition of cancer cell migration is crucial to prevent metastasis formation (Yamaguchi et al., 2005) as well as for inhibiting the development of hypertrophic scar tissue due to the over-production and migration of fibroblasts (Wang et al., 2008).

4 Conclusion

In this study, we exploited the processes of CTAB removal from gold nanorods and the concurring nanoparticle functionalization with a bioactive low-molecular weight (200 kDa) hyaluronan. The hybrid nanoconstructs of AuNR (-CTAB)/HA maintained a significant photothermal responsivity as bare nanorods, while nullifying the cytotoxic effect exhibited in prostate cancer cells and fibroblasts by the corresponding CTAB-capped analog nanoparticles. This approach for the post-synthesis treatment and biofunctionalization of gold nanorods is very promising for nanomedicine applications in the photothermal therapy of tumors as well as in the control of scar tissue formation in wound healing.

Data availability statement

The raw data supporting the conclusion of this article will be made available by the authors, without undue reservation.

Ethics statement

Ethical approval was not required for the studies on humans in accordance with the local legislation and institutional requirements because only commercially available established cell lines were used. Ethical approval was not required for the studies on animals in accordance with the local legislation and institutional requirements because only commercially available established cell lines were used.

Author contributions

AFo: data curation, investigation, and writing–original draft. BC: formal analysis, investigation, and writing–original draft. AFr: conceptualization, formal analysis, investigation, and writing–review and editing. LD: formal analysis, investigation, and writing–review and editing. AD: formal analysis, investigation, and writing–review and editing. CS: conceptualization, funding acquisition, methodology, supervision, and writing–review and editing.

Funding

The author(s) declare that financial support was received for the research, authorship, and/or publication of this article. This work has been partially funded by European Union (Next Generation EU), through the MUR (Ministero dell'università e della ricerca)-PNRR project SAMOTHRACE (ECS00000022). Moreover, the financial support by the MUR in the framework of PRIN2022-PNRR call under project CoMu4CaT is acknowledged.

Acknowledgments

The authors gratefully acknowledge the PON project Bionanotech Research and Innovation Tower (BRIT) and

BEST4U-PON R&I 2014-2020 e FSC, financed by the Italian Ministry for Education, University, and Research (MIUR). G. F. Indelli (BRIT) is acknowledged for technical support. Dr. Marcello Condorelli is kindly acknowledged for the Raman measurements. Prof. Salvatore Petralia is kindly acknowledged for the ZP measurements.

Conflict of interest

The authors declare that the research was conducted in the absence of any commercial or financial relationships that could be construed as a potential conflict of interest.

The author(s) declared that they were an editorial board member of Frontiers, at the time of submission. This had no impact on the peer review process and the final decision.

Publisher's note

Supplementary material

The Supplementary Material for this article can be found online at: https://www.frontiersin.org/articles/10.3389/fmats.2024.1381176/full#supplementary-material

References

Anselmo, A. C., and Mitragotri, S. (2016). Nanoparticles in the clinic. *Bioeng. Transl. Med.* 1, 10–29. doi:10.1002/btm2.10003

Bidian, C., Filip, G. A., David, L., Moldovan, B., Olteanu, D., Clichici, S., et al. (2023). Green synthesized gold and silver nanoparticles increased oxidative stress and induced cell death in colorectal adenocarcinoma cells. *Nanomaterials* 13, 1251. doi:10.3390/nano13071251

Bouhelier, A., Bachelot, R., Lerondel, G., Kostcheev, S., Royer, P., and Wiederrecht, G. P. (2005). Surface plasmon characteristics of tunable photoluminescence in single gold nanorods. *Phys. Rev. Lett.* 95, 267405. doi:10.1103/physrevlett.95.267405

Cannavà, C., De Gaetano, F., Stancanelli, R., Venuti, V., Paladini, G., Caridi, F., et al. (2022). Chitosan-hyaluronan nanoparticles for vinblastine sulfate delivery: characterization and internalization studies on K-562 cells. *Pharmaceutics* 14, 942. doi:10.3390/pharmaceutics14050942

Casas, J., Venkataramasubramani, M., Wang, Y., and Tang, L. (2013). Replacement of cetyltrimethylammoniumbromide bilayer on gold nanorod by alkanethiol crosslinker for enhanced plasmon resonance sensitivity. *Biosens. Bioelectron.* 49, 525–530. doi:10.1016/j.bios.2013.05.057

Cole, J. R., Mirin, N. A., Knight, M. W., Goodrich, G. P., and Halas, N. J. (2009). Photothermal efficiencies of nanoshells and nanorods for clinical therapeutic applications. *J. Phys. Chem. C* 113, 12090–12094. doi:10.1021/jp9003592

Da Silva, J. A., Netz, P. A., and Meneghetti, M. R. (2019). Growth mechanism of gold nanorods: the effect of tip–surface curvature as revealed by molecular dynamics simulations. *Langmuir* 36, 257–263. doi:10.1021/acs.langmuir.9b03235

Della Sala, F., Longobardo, G., Fabozzi, A., Di Gennaro, M., and Borzacchiello, A. (2022). Hyaluronic acid-based wound dressing with antimicrobial properties for wound healing application. *Appl. Sci.* 12, 3091. doi:10.3390/app12063091

Di Pietro, P., Strano, G., Zuccarello, L., and Satriano, C. (2016). Gold and silver nanoparticles for applications in theranostics. *Curr. Top. Med. Chem.* 16, 3069–3102. doi:10.2174/1568026616666160715163346

Foti, A., Calì, L., Petralia, S., and Satriano, C. (2023). Green nanoformulations of polyvinylpyrrolidone-capped metal nanoparticles: a study at the hybrid interface with biomimetic cell membranes and *in vitro* cell models. *Nanomaterials* 13, 1624. doi:10.3390/nano13101624

Garantziotis, S., and Savani, R. C. (2019). Hyaluronan biology: a complex balancing act of structure, function, location and context. *Matrix Biol.* 78-79, 1–10. doi:10.1016/j.matbio.2019.02.002

Gökce, H., and Bahçeli, S. (2013). The molecular structures, vibrational spectroscopies (FT-IR and Raman) and quantum chemical calculations of n-alkyltrimethylammonium bromides. *Opt. Spectrosc.* 115, 632–644. doi:10.1134/s0030400x13110076

Govindaraju, P., Todd, L., Shetye, S., Monslow, J., and Puré, E. (2019). CD44-dependent inflammation, fibrogenesis, and collagenolysis regulates extracellular matrix remodeling and tensile strength during cutaneous wound healing. *Matrix Biol.* 75-76, 314–330. doi:10.1016/j.matbio.2018.06.004

Greco, V., Naletova, I., Ahmed, I. M. M., Vaccaro, S., Messina, L., La Mendola, D., et al. (2020). Hyaluronan-carnosine conjugates inhibit Aβ aggregation and toxicity. *Sci. Rep.* 10, 15998. doi:10.1038/s41598-020-72989-2

He, J., Unser, S., Bruzas, I., Cary, R., Shi, Z., Mehra, R., et al. (2018). The facile removal of CTAB from the surface of gold nanorods. *Colloids Surfaces B Biointerfaces* 163, 140–145. doi:10.1016/j.colsurfb.2017.12.019

Jia, Y. P., Shi, K., Liao, J. F., Peng, J. R., Hao, Y., Qu, Y., et al. (2020). Effects of cetyltrimethylammonium bromide on the toxicity of gold nanorods both *in vitro* and *in vivo*: molecular origin of cytotoxicity and inflammation. *Small Methods* 4. doi:10.1002/smtd.201900799

Johnson, C. J., Dujardin, E., Davis, S. A., Murphy, C. J., and Mann, S. (2002). Growth and form of gold nanorods prepared by seed-mediated, surfactant-directed synthesis. *J. Mater. Chem.* 12, 1765–1770. doi:10.1039/b200953f

Li, Z., Huang, P., Zhang, X., Lin, J., Yang, S., Liu, B., et al. (2009). RGD-conjugated dendrimer-modified gold nanorods for *in vivo* tumor targeting and photothermal therapy. *Mol. Pharm.* 7, 94–104. doi:10.1021/mp9001415

Liu, Y., Chorniak, E., Odion, R., Etienne, W., Nair, S. K., Maccarini, P., et al. (2021). Plasmonic gold nanostars for synergistic photoimmunotherapy to treat cancer. *Nanophotonics* 10, 3295–3302. doi:10.1515/nanoph-2021-0237

Luo, Z., Dai, Y., and Gao, H. (2019). Development and application of hyaluronic acid in tumor targeting drug delivery. *Acta Pharm. Sin. B* 9, 1099–1112. doi:10.1016/j.apsb.2019.06.004

Meena, S. K., and Sulpizi, M. (2013). Understanding the microscopic origin of gold nanoparticle anisotropic growth from molecular dynamics simulations. *Langmuir* 29, 14954–14961. doi:10.1021/la403843n

Michalczyk, M., Humeniuk, E., Adamczuk, G., and Korga-Plewko, A. (2022). Hyaluronic acid as a modern approach in anticancer therapy-review. *Int. J. Mol. Sci.* 24, 103. doi:10.3390/ijms24010103

Movsesyan, A., Marguet, S., Muravitskaya, A., Béal, J., Adam, P.-M., and Baudrion, A.-L. (2019). Influence of the CTAB surfactant layer on optical properties of single metallic nanospheres. *J. Opt. Soc. Am. A* 36, C78. doi:10.1364/josaa.36.000c78

Naletova, L., Cucci, L. M., D'Angeli, F., Anfuso, C. D., Magrì, A., La Mendola, D., et al. (2019). A tunable nanoplatform of nanogold functionalised with angiogenin peptides for anti-angiogenic therapy of brain tumours. *Cancers* 11, 1322. doi:10.3390/cancers11091322

Nejabat, M., Samie, A., Ramezani, M., Alibolandi, M., Abnous, K., and Taghdisi, S. M. (2023). An overview on gold nanorods as versatile nanoparticles in cancer therapy. *J. Control. Release* 354, 221–242. doi:10.1016/j.jconrel.2023.01.009

Niidome, T., Yamagata, M., Okamoto, Y., Akiyama, Y., Takahashi, H., Kawano, T., et al. (2006). PEG-modified gold nanorods with a stealth character for *in vivo* applications. *J. Control. Release* 114, 343–347. doi:10.1016/j.jconrel.2006.06.017

Oliveira, C., Chaves, C. R., Bargiela, P., Da Rocha, M. D. G. C., Da Silva, A. F., Chubaci, J. F. D., et al. (2021). Surface studies of the chemical environment in gold nanorods supported by X-ray photoelectron spectroscopy (XPS) and *ab initio* calculations. *J. Mater. Res. Technol.* 15, 768–776. doi:10.1016/j.jmrt.2021.08.059

Orendorff, C. J., and Murphy, C. J. (2006). Quantitation of metal content in the silver-assisted growth of gold nanorods. *J. Phys. Chem. B* 110, 3990–3994. doi:10.1021/jp0570972

Palomba, F., Rampazzo, E., Zaccheroni, N., Malferrari, M., Rapino, S., Greco, V., et al. (2020). Specific, surface-driven, and high-affinity interactions of fluorescent hyaluronan with PEGylated nanomaterials. *ACS Appl. Mater. Interfaces* 12, 6806–6813. doi:10.1021/acsami.9b17974

Pérez-Juste, J., Pastoriza-Santos, I., Liz-Marzán, L. M., and Mulvaney, P. (2005). Gold nanorods: synthesis, characterization and applications. *Coord. Chem. Rev.* 249, 1870–1901. doi:10.1016/j.ccr.2005.01.030

Sanfilippo, V., Caruso, V. C. L., Cucci, L. M., Inturri, R., Vaccaro, S., and Satriano, C. (2020). Hyaluronan-metal gold nanoparticle hybrids for targeted tumor cell therapy. *Int. J. Mol. Sci.* 21, 3085. doi:10.3390/ijms21093085

Senbanjo, L. T., Aljohani, H., Majumdar, S., and Chellaiah, M. A. (2019). Characterization of CD44 intracellular domain interaction with RUNX2 in PC3 human prostate cancer cells. *Cell Commun. Signal.* 17, 80. doi:10.1186/s12964-019-0395-6

Su, G., Yang, C., and Zhu, J.-J. (2015). Fabrication of gold nanorods with tunable longitudinal surface plasmon resonance peaks by reductive dopamine. *Langmuir* 31, 817–823. doi:10.1021/la504041f

Tomasella, P., Sanfilippo, V., Bonaccorso, C., Cucci, L. M., Consiglio, G., Nicosia, A., et al. (2020). Theranostic nanoplatforms of thiolated reduced graphene oxide nanosheets and gold nanoparticles. *Appl. Sci.* 10, 5529. doi:10.3390/app10165529

Vigderman, L., and Zubarev, E. R. (2013). High-yield synthesis of gold nanorods with longitudinal SPR peak greater than 1200 nm using hydroquinone as a reducing agent. *Chem. Mater.* 25, 1450–1457. doi:10.1021/cm303661d

Villanueva-Flores, F., Castro-Lugo, A., Ramírez, O. T., and Palomares, L. A. (2020). Understanding cellular interactions with nanomaterials: towards a rational design of medical nanodevices. *Nanotechnology* 31, 132002. doi:10.1088/1361-6528/ab5bc8

Wang, J., Dodd, C., Shankowsky, H. A., Scott, P. G., and Tredget, E. E. (2008). Deep dermal fibroblasts contribute to hypertrophic scarring. *Lab. Investig.* 88, 1278–1290. doi:10.1038/labinvest.2008.101

Wang, L., Liu, Y., Li, W., Jiang, X., Ji, Y., Wu, X., et al. (2011). Selective targeting of gold nanorods at the mitochondria of cancer cells: implications for cancer therapy. *Nano Lett.* 11, 772–780. doi:10.1021/nl103992v

Wittmann, M., Henze, K., Yan, K., Sharma, V., and Simmchen, J. (2023). Rod-shaped microparticles — an overview of synthesis and properties. *Colloid Polym. Sci.* 301, 783–799. doi:10.1007/s00396-023-05111-3

Yamaguchi, H., Wyckoff, J., and Condeelis, J. (2005). Cell migration in tumors. *Curr. Opin. Cell Biol.* 17, 559–564. doi:10.1016/j.ceb.2005.08.002

Yao, L., Bojic, D., and Liu, M. (2023). Applications and safety of gold nanoparticles as therapeutic devices in clinical trials. *J. Pharm. Analysis* 13, 960–967. doi:10.1016/j.jpha.2023.06.001

Zhang, L., Wang, L., Hu, Y., Liu, Z., Tian, Y., Wu, X., et al. (2013). Selective metabolic effects of gold nanorods on normal and cancer cells and their application in anticancer drug screening. *Biomaterials* 34, 7117–7126. doi:10.1016/j.biomaterials.2013.05.043

Zhang, R., Kiessling, F., Lammers, T., and Pallares, R. M. (2022). Clinical translation of gold nanoparticles. *Drug Deliv. Transl. Res.* 13, 378–385. doi:10.1007/s13346-022-01232-4